Hindawi
Advances in Multimedia
Volume 2022, Article ID 1037716, 12 pages
https://doi.org/10.1155/2022/1037716

Research Article

Building Crack Detection Based on Digital Image Processing Technology and Multiscale Feature Analysis Automatic Detection Algorithm

Chenguang Liu

The Audit Department, Shandong College of Arts, Jinan 250004, Shandong, China

Correspondence should be addressed to Chenguang Liu; z00107@sdca.edu.cn

Received 13 March 2022; Revised 29 April 2022; Accepted 6 May 2022; Published 23 May 2022

Academic Editor: Qiangyi Li

At present, the monitoring of concrete cracks is still mainly carried out by engineering personnel using simple mechanical monitoring instruments. The human inspection will undoubtedly be interfered by the individual's psychological, physical, and external conditions, and there may also be unobjective emotions, so it is impossible to ensure that the quality of the detection is up to standard and accurate. This paper combines digital image processing technology and multiscale feature analysis automatic detection algorithm to construct an intelligent building structure crack detection system. Moreover, this paper proposes an enrichment scheme for the unknown partially entangled states of building microparticles and utilizes the entanglement exchange process based on the Raman interaction of two building microparticles. The experimental results show that the automatic detection method of building cracks based on digital image processing technology and multiscale feature analysis has a good effect.

1. Introduction

The factors that cause cracks in concrete include the difference in the composition of the material of the structure itself, the difference in the building system, and even the influence of geographical environment and climatic factors. In general, the types of concrete cracks can be divided into [1] (1) cracks caused by changes in the shape of the building; (2) cracks caused by too much weight; (3) cracks caused by insufficient quality; (4) cracks caused by irregular operation during construction. Among these types of cracks, the largest proportion is due to the change in the shape of the concrete in the building. The quality and safety of the building are not affected by the change in the shape of the concrete resulting in larger cracks; that is, the building's bearing capacity has not changed much. However, the appearance of cracks caused a great psychological barrier to the occupants, which affected the handover of the whole project [2]. In addition, the cracks in the building will cause the Party A of the construction project to reject the feeling, which is not conducive to the continued cooperation of the construction team in the future, and will have an adverse impact on the entire work team. Moreover, building cracks are a major stain on engineering quality. First, there is a clear requirement in the code of practice for construction projects to reduce the occurrence of cracks. Second, there is no agreement that cracks can appear in buildings in the current project quality inspection specifications. Third, users will also not accept buildings with obvious cracks. In other words, this problem also reflects that the technical level of the engineering industry is not up to the mark, and the cracks have a bad impact on the beauty and normal use of the entire building and even threaten the property and life of users [3]. Cracks in concrete also lead to great adverse effects in terms of economy. For example, the engineering team had to carry out a series of remedial measures for cracked buildings, such as reinforcement and maintenance, and the cost of these two measures was huge. Some foreign professionals estimate that the annual remediation funds for facilities are now calculated at 8 billion yuan. Therefore, strengthening the detection of the causes of concrete cracks and monitoring and detection is the top priority of

accurately identifying construction quality projects and reducing project damage. Moreover, if the occurrence of cracks cannot be accurately detected on time, a series of monitoring methods are not complete, and the analysis of data is not deep enough, then solving the crack problem is still only an extravagant hope.

This paper combines digital image processing technology and multiscale feature analysis automatic detection algorithm to construct an intelligent building structure crack detection system to improve the crack detection effect of building structures.

2. Related Work

The particularity of concrete material determines that concrete is widely used in the construction industry, and its own flow-plastic state can configure concrete structural components of different shapes. The advantages of concrete are high strength and good durability after forming [4]. In recent years, the scale of the project has been expanding, and concrete materials have been widely used. In the high-quality life, in order to meet the needs of users, the building structure has become particularly complex, resulting in the increasingly prominent crack problem in the engineering structure, which has plagued the personnel in the construction industry for a long time. This is due to the shortcomings of concrete materials, its tensile strength is very low, and its own defects determine that cracks are inevitable in structural construction [5]. This characteristic is also revealed in the microscopic study of concrete materials by modern science. It is enough to control the cracks within the acceptable range of people. The pursuit of high standards and high requirements of sensory quality is bound to bring huge economic costs. In general, concrete has characteristics that other materials do not have; that is, it is allowed working with cracks in the structure, but it is not indulgent, but it is controlled within a reasonable range under the condition of ensuring the safety of the structure [6]. The structure itself is affected by various external environments, construction conditions, and constraints between components. In the design stage, reasonable stress construction measures should be adopted. In the construction stage, the quality should be strictly controlled, construction management should be strengthened, and reasonable construction techniques should be adopted, improved, and solved [7].

With the development of science and technology, people's understanding of the microstructure of materials continues to deepen, and scientists put forward the theory of concrete structure on the basis of phenomenological theory. In the process of research, people are more and more deeply aware of the influence of concrete material itself on cracks, and the research on concrete material itself is also deepening [8]. Xiong et al. [9] applied the finite element method to study the shrinkage and creep of concrete. Black [10] believes that the heat of structural hydration causes the volume change of the concrete structure, which generates internal stress under the condition of external constraints, which in turn leads to the early cracking of the concrete structure. In [11], when studying the relationship between the degree of structural restraint and the early deformation of concrete, and the transition state mechanical properties of hardened concrete, it was found that the temperature point of view in the traditional view is not comprehensive for the standard of crack risk, so the early concrete is proposed. Cracking is caused by volume changes caused by the heat of hydration of concrete. They divided the cracks into concrete cracks in the expansion stage and concrete cracks in the shrinkage stage.

Photogrammetry is the analysis of two-dimensional images obtained by measuring cameras or nonmeasuring cameras to determine the position, shape, size, and even the movement of objects in three-dimensional space [12]. Measuring cameras are specially designed and manufactured for photogrammetry, with stable mechanical structure and good optical performance [13], but high prices. Nonmeasuring cameras are photographic equipment such as ordinary digital cameras, which are relatively cheap. Photogrammetry technology is a branch of surveying and mapping, so for a long time, most of the work on photogrammetry has used aerial photography to obtain topographic information and draw topographic maps [14]. Some people use measuring cameras or nonmeasuring cameras to photograph objects at a close distance and then process and analyze the obtained two-dimensional images to obtain various information about the object, which is digital close-range photogrammetry technology. Digital close-range photogrammetry technology is applied to the field of crack detection. Through the coordinate transformation analysis of photographic graphics, a two-dimensional coordinate system and a three-dimensional coordinate system are established to obtain buildings' basic information [15].

The crack width detector collects the target image through the front-end camera and transmits it to the LCD for display and measurement. According to the different measurement methods, it is divided into two types: manual reading method and automatic measurement method. There is a scale on the screen of the manual reading method of the crack width detector. When measuring, the crack width is read out according to the distance between the lines on the screen. Compared with the crack microscope method, the use of liquid crystal display instead of human eye observation reduces the reading errors caused by labor intensity and visual fatigue to a certain extent [16].

Reference [17] is based on the traditional digital close-range photogrammetry method to measure the crack width. A camera is used to shoot the crack vertically. Every time the position of the camera is changed, it needs to be recalibrated. It is proposed to project the crack edge curve to the space plane, a stereo vision method for recovering the three-dimensional coordinates of the crack edge, and its feasibility is verified by experiments. Pei et al. [18] proposed a three-dimensional cross-direction shooting method that uses two cameras to shoot from different angles, which is used to detect road pavement cracks, and obtains more information than the monocular method.

3. Microscopic Finite Element Particle Recognition of Digital Buildings

Due to the main role of entanglement in the process of building finite element particle information, the preparation of various types of entangled states has always been a hot issue in the research of building finite element particle information. In addition to the method of entangling the originally unrelated quantities through interaction, there is another kind of method to obtain the entangled state, which is to obtain the entangled state we need from the entangled state, and entanglement exchange is such a method.

Another way is to get the maximally entangled state we need from a series of partially entangled states: This operation is called entanglement concentration for pure states and entanglement purification or entanglement distillation for mixed partially entangled states. The generation of some entangled states in the experiment may be due to the imperfection of the experimental scheme, or it may be due to the influence of the loss during the entanglement transmission process. However, in the process of building finite element particle information processing based on entangled state, a large part of it is based on the maximum entangled state. Entanglement enrichment or entanglement purification is a class of methods that aim to obtain a small number of maximally entangled states from a large sample of partially entangled states through local manipulation and classical communication.

So far, many theoretical and experimental schemes for entanglement purification and entanglement enrichment have been proposed. Many physical systems can be used to achieve entanglement purification or concentration. Experiments with entanglement purification in these schemes are mainly limited to the use of linear optical elements such as beam splitters. A scheme to achieve entanglement purification using photonic states has also been proposed. And entanglement condensation in continuous variable systems has also received attention. Entanglement exchange can also be used to achieve entanglement enrichment. The entanglement concentration and entanglement purification of architectural finite element particle state have also received attention. At present, many entanglement concentration and purification schemes for architectural finite element particle state have been proposed, but its experimental realization is still being explored. Therefore, it is also a major research trend to find an experimentally easy-to-implement solution for purification or enrichment of entangled states of architectural finite element particles.

In cavity QED systems, the decay of cavity modes, the thermal field effect caused by the excitation of the cavity field, and the decoherence caused by the decay of spontaneous radiation of architectural finite element particles are the main obstacles to the current experiments of cavity QED systems. In the literature, a condensed scheme of the entangled state of architectural finite element particles is proposed. They use a classical field and a cavity mode to simultaneously couple the same transition of two architectural finite element particles and obtain two under the condition of strong driving field approximation and large detuning. The effective interaction Hamiltonian of each building finite element particle results in the state evolution required in the entanglement enrichment scheme. In their entanglement enrichment scheme of this architectural finite element particle state, cavity attenuation and thermal field effects are eliminated. Inspired by this scheme, we propose an entanglement enrichment scheme for architectural finite element particle states. Combining the finite element particle and the external classical field, the effective interaction between the ground states of the two building finite element particles is analyzed, and the evolution process of the building finite element particle state is obtained. Since the cavity field is not excited and the excited states of the architectural finite element particles do not participate in the interaction, in our scheme, the decay of the cavity field, the decoherence caused by the thermal field, and the spontaneous emission of the architectural finite element particles are all suppressed. And compared with the schemes in the literature, our scheme only needs to select the architectural finite element particle velocity without adjusting the Rabi frequency of the classical field to complete the entanglement enrichment process, which shows that the operation steps in our scheme are simplified.

We first introduce the architectural finite element particle and field action forms required in our entanglement enrichment scheme. Consider two three-level Λ-type architectural finite element particles, each of which has two metastable states $|g\rangle$ and $|e\rangle$ and an excited state $|h\rangle$, as shown in Figure 1. The single-mode cavity field-driven dipole-allowed transition is $|g\rangle \longrightarrow |h\rangle$ with annihilation operator a, and the monochromatic laser field coupled dipole transition is $|e\rangle \longrightarrow |h\rangle$. Under the dipole approximation and the rotating wave approximation, the Hamiltonian of the system composed of the building finite element particles and fields in the interaction picture is ($\hbar = 1$).

In the above figure, the single-mode cavity field coupling transition is $|g\rangle \longrightarrow |h\rangle$, and the optical field-driven transition is $|e\rangle \longrightarrow |h\rangle$.

$$H_1 = \sum_{j=2}^{3}\left(ga e^{-i\Delta t}\left|h_j\right\rangle t\left\langle g_j\right| + \Omega e^{-i\Delta t}\left|h_j\right\rangle n\langle q e_j| + H.c.\right). \quad (1)$$

Among them, *H.c.* stands for complex conjugate. g and Ω are the Rabi frequencies of the cavity mode and the laser field, respectively, which are taken as real numbers for the simplicity of the calculation. $\Delta = \omega_c - \omega_{hg} = \omega_L - \omega_{he}$ is the detuning of the two fields and their respective transitions, and we assume that the detuning is large, that is, $|\Delta| \gg g, \Omega$; ω_{hg} and ω_{he} are the transition frequencies of the architectural finite element particles; ω_c and ω_L are the frequencies of the cavity and laser fields, respectively. For the simplicity of the calculation, we assume that the coupling

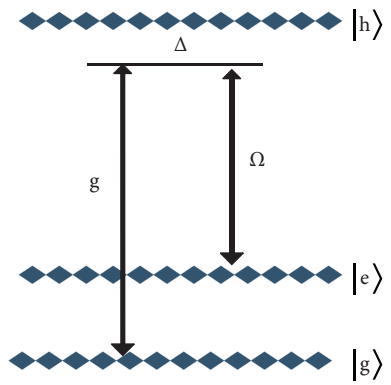

Figure 1: Schematic illustration of the Raman interaction of three-level Λ-type architectural finite element particles and cavity fields and laser fields.

constants of the two building finite element particles and fields are the same. After adiabatically eliminating the excited states of the building finite element particles, we get the following effective Hamiltonian:

$$H_2 = \sum_{j=2}^{3}\left(\frac{g^2}{\Delta}a^{\dagger}a\left|g_j\right\rangle t\left\langle g_j\right| + \frac{\Omega^2}{\Delta}\left|e_j\right\rangle n\left\langle e_j\right| + \frac{g\Omega}{\Delta}a^{\dagger}\left|g_j\right\rangle q\left\langle e_j\right| + \frac{g\Omega}{\Delta}a\left|e_j\right\rangle h\left\langle g_j\right|\right). \tag{2}$$

This is the interaction between two metastable states of architectural finite element particles caused by Raman interaction. We assume that the cavity field is initially in a vacuum state, and with transfer into the interaction frame rotated with $H_0 = \Omega^2/\Delta\,(|e_2\rangle t\langle e_2| + |e_3\rangle n\langle qe_3|)$, the above effective Hamiltonian becomes the following form:

$$H_3 = \sum_{j=2}^{3}\left(\lambda_1 e^{-i\lambda_2 t}a^{\dagger}\left|g_j\right\rangle t\left\langle e_j\right| + \lambda_1 e^{i\lambda_2 t}a\left|e_j\right\rangle n\left\langle qg_j\right|\right). \tag{3}$$

Among them, $\lambda_1 = g\Omega/\Delta, \lambda_2 = \Omega^2/\Delta$. When $\lambda_2 \gg \lambda_1$, that is, when the laser field is driven by a strong field, then there is $\Omega \gg g$. We can obtain the following effective Hamiltonian by using $H_e = -iH_3(t)\int_0^t H_3(t')\mathrm{d}t'$ and ignoring the high-frequency oscillation term:

$$H_e = \lambda\left(\left|e_2\right\rangle t\left\langle e_2\right| + \left|e_3\right\rangle n\left\langle qe_3\right|\right) + \lambda\left(s_2^{+}s_3^{-} + s_3^{+}s_2^{-}\right). \tag{4}$$

Among them, $\lambda = g^2/\Delta$, the building finite element particle operator is $s_j^{+} = |e_j\rangle t\langle ng_j|$, and the building finite element particle operator is $s_j^{-} = |g_j\rangle t\langle ne_j|$. From this expression, it can be seen that, during this interaction, the cavity field is in a state of virtual excitation. Therefore, the cavity field is always in its vacuum state during the whole action process. Using this effective Hamiltonian, we can obtain the state evolution of the architectural finite element particles as follows:

$$\begin{aligned}
&\left|e_2\right\rangle\left|e_3\right\rangle \longrightarrow e^{-i2\lambda t}\left|e_2\right\rangle\left|e_3\right\rangle,\\
&\left|e_2\right\rangle\left|g_3\right\rangle \longrightarrow e^{-i\lambda t}\left[\cos(\lambda t)\left|e_2\right\rangle\left|g_3\right\rangle - i\sin(\lambda t)\left|g_2\right\rangle\left|e_3\right\rangle\right],\\
&\left|g_2\right\rangle\left|e_3\right\rangle \longrightarrow e^{-i\lambda t}\left[\cos(\lambda t)\left|g_2\right\rangle\left|e_3\right\rangle - i\sin(\lambda t)\left|e_2\right\rangle\left|g_3\right\rangle\right],\\
&\left|g_2\right\rangle\left|g_3\right\rangle \longrightarrow \left|g_2\right\rangle\left|g_3\right\rangle.
\end{aligned} \tag{5}$$

As we will see later, this evolution of the architectural finite element particle system can be used to realize the condensed scheme of the unknown entangled state of the architectural finite element particle.

In the following, we will introduce in detail the process of condensing the unknown entangled state of architectural finite element particles. We assume that there are four three-level Λ-type building finite element particles, and these four building finite element particles are in the following two nonmaximally entangled states:

$$\begin{aligned}
|\psi\rangle_{12} &= A\left|e_1\right\rangle\left|g_2\right\rangle + B\left|g_1\right\rangle\left|e_2\right\rangle,\\
|\psi\rangle_{34} &= C\left|e_3\right\rangle\left|g_4\right\rangle + D\left|g_3\right\rangle\left|e_4\right\rangle.
\end{aligned} \tag{6}$$

Among them, A, B, C, and D are unknown normalization coefficients that satisfy $A^2 + B^2 = 1$ and $C^2 + D^2 = 1$. In addition, we mainly consider the concentration of the following special partially entangled states; that is, the coefficients of these partially entangled states also satisfy the relation $A/B = D/C \neq 1$. This formula shows that neither $|\psi\rangle_{12}$ nor $|\psi\rangle_{34}$ is the maximum entangled state of the two building finite element particles.

In order to obtain a maximum entangled state of two-building finite element particles from these two partially entangled states, a cavity needs to be introduced at the location of Charles. Then, Charles sends his two architectural finite element particles 2 and 3 into the cavity to interact with the laser field. This mode of action is the interaction process between building finite element particles and fields that we introduced earlier. In the strong driving limit, this interaction is described by the effective Hamiltonian in equation (4). The possible state evolution of architectural finite element particles 2 and 3 is described by equation (5). Using this state evolution, the evolution of the

joint initial state of the four architectural finite element particles is

$$\begin{aligned}&\left(A|e_1\rangle|g_2\rangle + B|g_1\rangle|e_2\rangle\right)\left(C|e_3\rangle|g_4\rangle + D|g_3\rangle|e_4\rangle\right)\\&\longrightarrow A\ D|e_1\rangle|e_4\rangle|g_2\rangle|g_3\rangle + BC|g_1\rangle|g_4\rangle e^{-i2\lambda t}|e_2\rangle|e_3\rangle\\&+ AC|e_1\rangle|g_4\rangle e^{-i\lambda t}\left[\cos(\lambda t)|g_2\rangle|e_3\rangle - i\ \sin(\lambda t)|e_2\rangle|g_3\rangle\right]\\&+ B\ D|g_1\rangle|e_4\rangle e^{-i\lambda t}\left[\cos(\lambda t)|e_2\rangle|g_3\rangle - i\ \sin(\lambda t)|g_2\rangle|e_3\rangle\right].\end{aligned} \tag{7}$$

After the action, a joint measurement is made of the states of the building finite element particles 2 and 3. If the building finite element particles 2 and 3 are detected to be in two different states, that is, the building finite element particles 2 and 3 are detected in state $|g_2\rangle|e_3\rangle$ or $|e_2\rangle|g_3\rangle$, the corresponding states of atoms 1 and 4 will collapse to

$$|\psi\rangle_{14} = e^{-i\lambda t}N_1\left[\cos(\lambda t)AC|e_1\rangle|g_4\rangle - i\ \sin(\lambda t)B\ D|g_1\rangle|e_4\rangle\right]. \tag{8}$$

Alternatively, there is

$$|\psi\rangle'_{14} = e^{-i\lambda t}N_2\left[\cos(\lambda t)B\ D|g_1\rangle|e_4\rangle - i\ \sin(\lambda t)AC|e_1\rangle|g_4\rangle\right]. \tag{9}$$

Among them, the normalization factor is

$$\begin{aligned}N_1 &= \left[\cos^2(\lambda t)A^2C^2 + \ \sin^2(\lambda t)B^2D^2\right]^{-(1/2)},\\N_2 &= \left[\cos^2(\lambda t)B^2D^2 + \ \sin^2(\lambda t)A^2C^2\right]^{-(1/2)}.\end{aligned} \tag{10}$$

By choosing the velocity of the building finite element particles to make the interaction time $t = \pi/4\lambda$ and using the initial condition $A\ C = B\ D$, the states of the building finite element particles 1 and 4 are

$$|\Phi\rangle_{14} = \frac{1}{\sqrt{2}}\left(|e_1\rangle|g_4\rangle - i|g_1\rangle|e_4\rangle\right). \tag{11}$$

Alternatively, there is

$$|\Phi\rangle_{14}{}' = \frac{1}{\sqrt{2}}\left(|g_1\rangle|e_4\rangle - i|e_1\rangle|g_4\rangle\right). \tag{12}$$

If the building finite element particles 2 and 3 are measured to be in the same state, that is, the state of the building finite element particles 2 and 3 is $|e_2\rangle|e_3\rangle$ or $|g_2\rangle|g_3\rangle$, it means that the rectification concentration process is lost. We need to restart the interaction until we finally measure that the building finite element particles 2 and 3 are in one of two different metastable states, respectively. With $|e_2\rangle|g_3\rangle, |g_2\rangle|e_3\rangle_0$ for any one of these cases where entanglement concentration may be obtained, after a rotation operation, the states of building finite element particles 1 and 4 will become the following two maximum entangled states of building finite element particles:

$$|\phi\rangle_{14} = \frac{1}{\sqrt{2}}\left(|e_1\rangle|g_4\rangle + |g_1\rangle|e_4\rangle\right). \tag{13}$$

The probability of obtaining the maximum entangled state of the finite element particles of the two buildings is $P = 2A^2C^2$, where the factor 2 is derived from the detection results $|e_2\rangle|g_3\rangle$ and $|g_2\rangle|e_3\rangle$, which correspond to the maximum entangled state of the finite element particles of the same two buildings. It can be seen from this that the two building finite element particles 1 and 4, which have no interaction originally, are in the maximum entangled state of two building finite element particles after the entanglement exchange. The realization of the entanglement exchange process here is achieved by the Raman interaction of the two architectural finite element particles and the cavity field as well as the laser field and under the strong driving effect of the laser field. This scheme achieves the entanglement enrichment of a maximum entangled state of two building finite element particles from two partially entangled states of four building finite element particles.

Our entanglement enrichment scheme has a certain capacity for fault tolerance, which is manifested as a small error in the coefficients of the initial two partial entangled states, which has little effect on the fidelity of the final maximum entangled state of two-building finite element particles obtained by our scheme, which can be almost ignored. Among them, we assume that this small error comes from the shadow of not being able to send two building finite element particles into the air at the same time. Consider the following special case $A = D$, $B = C$, the relation $A/B = D/C \neq 1$ always holds. When there is such a small error, for example, due to this small error, the coefficient A in it has a deviation, that is, $D = A + k\ A$, where k is a small constant. With this little error, we finally obtain the state of the building finite element particles 1 and 4 for the entanglement enrichment process after the rotation operation as

$$|\phi\rangle'_{14} = \frac{1}{\sqrt{N}}\left(\sqrt{1 - A^2(1+k)^2}\,|e_1\rangle|g_4\rangle + (1+k)\sqrt{1 - A^2}\,|g_1\rangle|e_4\rangle\right). \tag{14}$$

Among them, $N = 1 + (1+k)^2 - 2A^2(1+k)^2$, which is the requirement of the normalization condition. The fidelity of the entanglement enrichment process is defined as the square of the modulus of the inner product of $|\phi\rangle_{14}$ between the state we obtained and the maximum entangled state of the two building finite element particles, that is, $F = |\langle\phi'_{14}\|\phi_{14}\rangle|^2$, and the result of the calculation is

$$F = \frac{\left[\sqrt{1 - A^2(1+k)^2} + (1+k)\sqrt{1 - A^2}\right]^2}{2\left[1 + (1+k)^2 - 2A^2(1+k)^2\right]}. \tag{15}$$

If $A = 0.7$, $k = 0.1$, then the fidelity is $F \approx 0.989$. This result shows that small errors in the coefficients of the initial two partially entangled states have little effect on the fidelity of the maximally entangled state we finally obtain for the two building finite element particles.

The experimental feasibility of this scheme is analyzed below. We take the two states of the main building finite element particles of the Rydberg building finite element particles, 50 and 51, respectively, to represent our metastable

and excited states. The characteristic time of spontaneous emission of architectural finite element particles is $T_r = 30$ ms, and the two metastable $|g\rangle$ and $|e\rangle$ of architectural finite element particles are the two fine sublevels of the ground state. The resonance frequency of building finite element particles with $|g\rangle \longrightarrow |h\rangle$ transition is about 51.1 GHz. For the Rydberg building finite element particles interacting with the high-quality factor cavities, the coupling constant between the building finite element particles and the hull can reach $g \approx 2\pi \times 50$ kHz, and the decay time of the cavity is $t_c = 1.5$ milliseconds. By choosing $\Omega = 10$ g and $\Delta = 100$ g, the strong driving conditions $\Delta \gg \Omega$, g and $\Omega \gg g$ can be satisfied at the same time. In this case, the effective combination constant of the building finite element particle-cavity is $\lambda = 0.01$ g. In this scheme, the probability of the excitation field is a small xu, that is, $P_c = 0.01$. Therefore, the effective reduction time of the cavity is $T_c = P_c^{-1} t_c = 150$ seconds. In this entanglement enrichment scheme, the excited states of the architectural finite element particles do not participate in the interaction and the cavity field is also virtually excited. Spontaneous emission of architectural finite element particles, cavity attenuation, and the resulting decoherence due to thermal field effects have no effect on our results of entanglement enrichment. Based on the above reasons, our method of condensing the rectified state of finite element particles of unknown buildings is experimentally feasible.

Geometric parameters are the most basic properties of cracks. The key to identifying pavement cracks is to calculate the geometric parameters of cracks. In order to facilitate the implementation of subsequent work by road maintenance personnel, it is necessary to calculate relevant geometric parameters for different types of cracks. Among them, the linear fracture needs to consider its length and width parameter information, and the network fracture is mainly concerned with its minimum circumscribed rectangular area.

According to the linear characteristics of cracks, before calculating the length and width of linear cracks, it is necessary to refine the cracks, that is, extract the skeleton of the crack peak without changing the crack peak profile and obtain a single-pixel wide crack.

The extraction of the skeleton is done by erosion and opening operations. We set A as the image to be processed and B as the structural element, and the skeleton is as follows:

$$S(A) = \bigcup S_k(A), \quad k = 1, 2, \ldots, K. \tag{16}$$

Among them, $S_k(A)$ is the skeleton subset; the formula is as follows:

$$S_k(A) = A \Theta kB - (A \Theta kB) \circ B. \tag{17}$$

In formula (2), $A \Theta kB$ is the consecutive k times of erosion of A, K is the last iterative step before A is eroded into an empty set, and the expression is

$$K = \max\{k | A \Theta kB \neq \varnothing\}. \tag{18}$$

If the actual length of each pixel is μ ($\mu = 0.92$ mm in this data set), and the total number of pixels l after refinement is calculated, the length of the linear crack is $L = \mu l$.

The linear crack width is divided into minimum width, maximum widt,h and average width. In this paper, the vertical line method based on the split skeleton is used to calculate the width. The basic idea is to make the vertical line of the crack, determine the two intersection points $A(x_1, y_1), B(x_2, y_2)$ of the vertical line and the edge of the crack, and use the distance formula between the two points to calculate the width of the local area as

$$d = \sqrt{(x_1 - x_2)^2 + (y_1 - y_2)^2}. \tag{19}$$

To obtain n pixel width samples $\{d_i | i \geq 1 \& i \leq n\}$ for linear cracks, the minimum and maximum widths of cracks are, respectively:

$$\begin{cases} d_{\min} = \min(d_i), \\ d_{\max} = \max(d_i). \end{cases} \tag{20}$$

The number of unrefined crack pixels E is calculated:

$$E = \sum_{x=1}^{M} \sum_{y=1}^{N} f(x, y). \tag{21}$$

Then, the actual area of the linear crack is $Q = \mu E$, and the average crack width can be expressed as $d_{\text{avg}} = Q/L$.

We take the figure as an example to calculate the parameters, calculate the pavement damage index PCI and the crack rate C_K according to the formula, and make the final pavement evaluation according to the table.

Usually, for network cracks, the area surrounded by the outermost cracks is used to measure the size of the cracks, and then the damage degree of the pavement cracks is evaluated. The maximum value X_1 and minimum value X_2 of the coordinates projected on the X axis of the crack and the maximum value Y_1 and the minimum value Y_2 of the coordinates projected on the Y axis are recorded.

The calculation of the mesh crack area is

$$S = \mu^2 (X_2 - X_1) \times (Y_2 - Y_1). \tag{22}$$

In the formula, μ^2 represents the proportion of the actual area occupied by a pixel.

4. Research on Building Crack Detection considering Digital Image Processing Technology Combined with Multiscale Feature Analysis Automatic Detection Algorithm

The overall design of the system is shown in Figure 2, which is mainly composed of machine vision system and embedded Linux system. This paper combines the algorithm of the third part to perform digital image processing to detect building cracks.

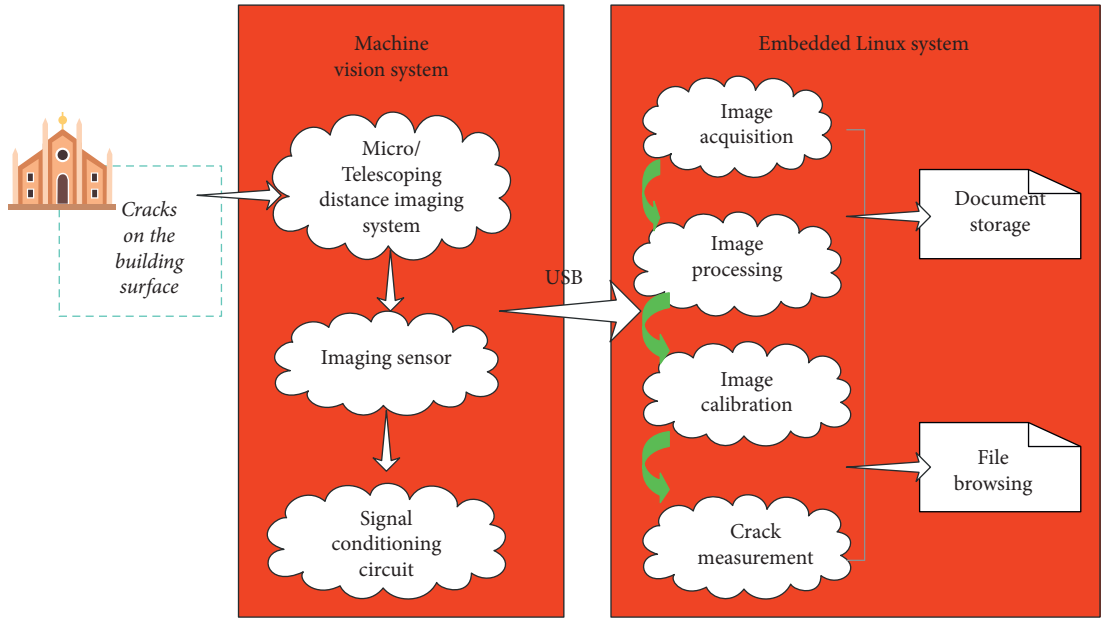

Figure 2: Overall scheme of the system.

Two classification criteria are used to compare the effect of sample discarding on crack detection. The classification methods and results of the two methods are shown in Figures 3(a) and 3(b). The 90 original images are expanded to 1350 images through data enhancement, and they are automatically segmented and marked according to the two classification standards mentioned above. Moreover, this paper randomly selects 50,000 marked positive and negative samples as data set 1 and data set 2. The number of positive and negative samples is the same to ensure the balance of the samples.

The model in this paper is based on the network structure shown in Figure 4 below. Figures 4(a) and 4(b) are the network structure diagrams of the Cha network and AlexNet, respectively. The input size of the Cha network is $256 \times 256 \times 3$ pixels, and the three-layer convolutional receptive fields in the network are 20×20 and 15 pixels, respectively, with 15×15 and 10×10 sizes. The input size of AlexNet is $227 \times 227 \times 3$ pixels, and the receptive field of the first layer convolution is 11×11, and the rest of the convolutional receptive fields are 3×3.

The processed image is shown in Figure 5.

The establishment of this index can evaluate the influence of various factors on the final crack detection result in the framework of concrete crack detection based on convolutional neural network. Moreover, the distance index established based on the large image can more intuitively reflect the gap between the crack marked on the original image and the real crack than the evaluation index based on the small image. Therefore, a large image with poor detection effect can be directly found according to this distance index. Through the marking of cracks on the large image, it is faster and clearer to judge the situation of the wrong parts, such as shadows, smears, etc., which are easily misjudged in the sample. It is difficult to distinguish multiple categories from the small sample image, but these parts can be clearly judged on the large image.

On the basis of the above research, this paper verifies the effect of the building crack detection method based on digital image processing technology and multiscale feature analysis automatic detection algorithm. In this paper, several sets of crack images are used for experimental research, and the effectiveness of the method in this paper is counted, and the results shown in Table 1 and Figure 6 are finally obtained.

The above research verifies that the automatic detection method of building cracks based on digital image processing technology and multiscale feature analysis automatic detection algorithm proposed in this paper has a good effect.

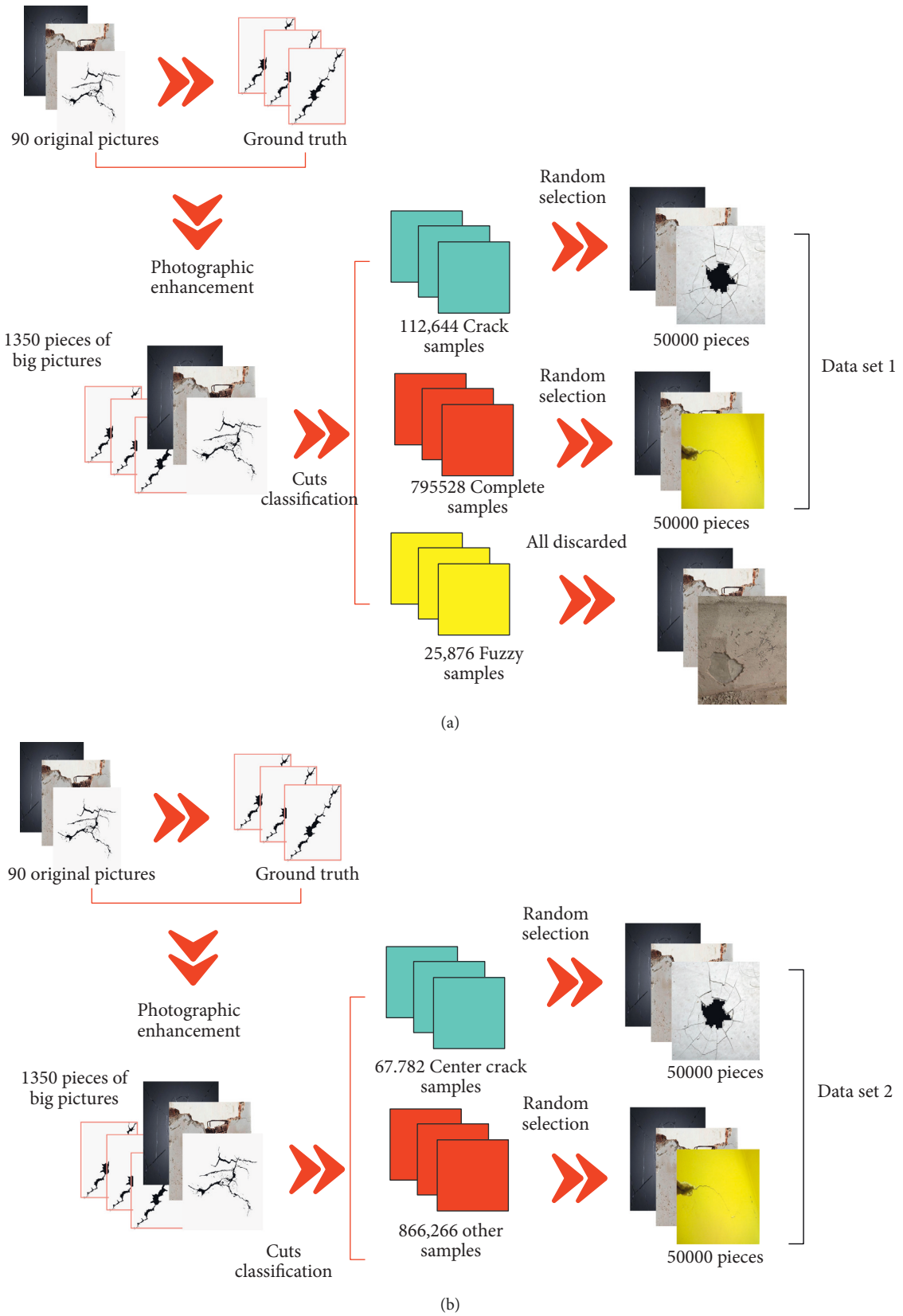

Figure 3: Two classification methods. (a) Dataset 1, (b) Dataset 2.

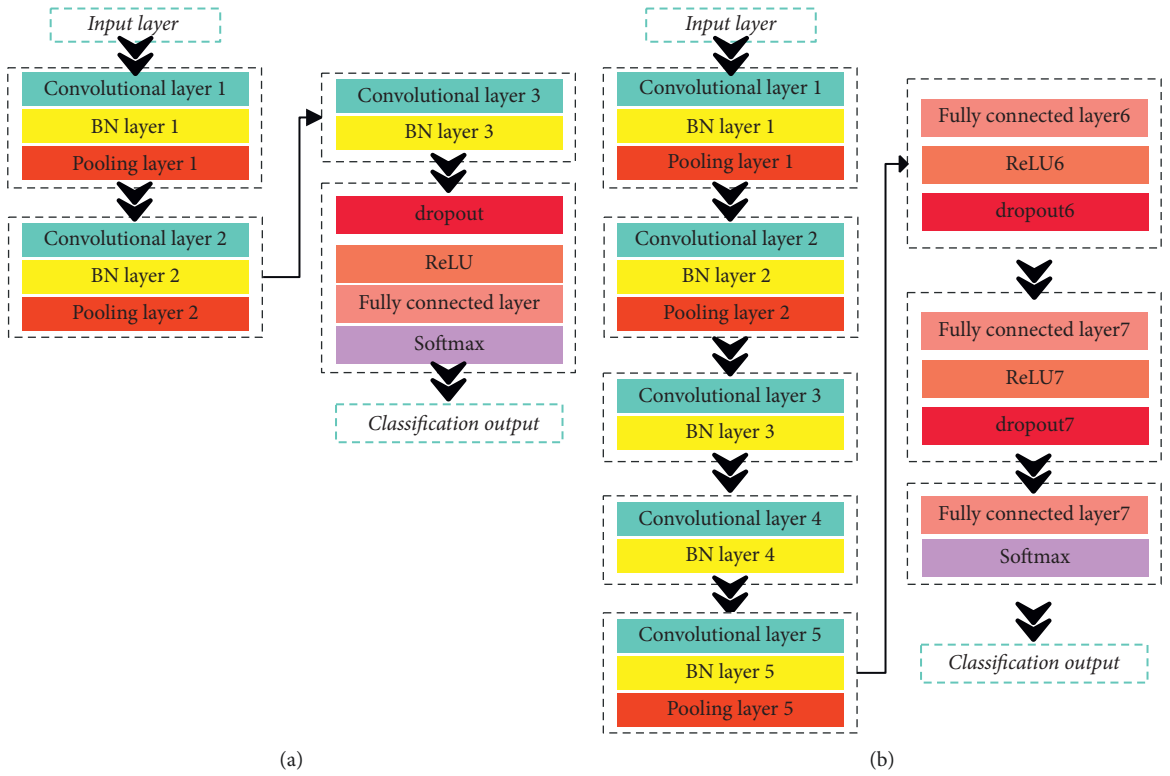

Figure 4: System network architecture diagram. (a) Cha network architecture, (b) AlexNet network architecture diagram.

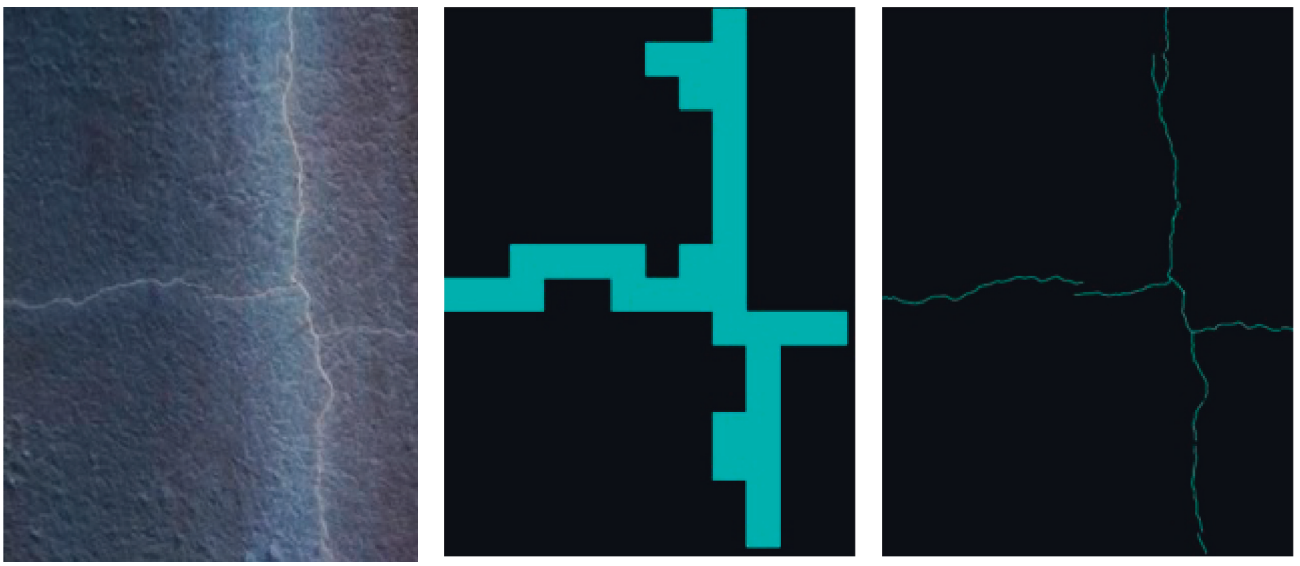

(a) (b) (c)

Figure 5: Continued.

(d)

Figure 5: Image after processing. (a) Original image, (b) image after tagging, (c) ground truth, (d) bold ground truth.

Table 1: The effect verification of the automatic detection method of building cracks based on digital image processing technology and multiscale feature analysis automatic detection algorithm.

Num	Crack detection	Num	Crack detection	Num	Crack detection
1	85.5	20	76.9	38	76.8
2	79.4	21	86.9	39	82.2
3	80.2	22	81.9	40	79.9
4	79.1	23	84.0	41	76.0
5	81.3	24	83.1	42	81.0
6	79.9	25	80.8	43	82.5
7	80.5	26	81.2	44	85.1
8	86.1	27	78.8	45	82.6
9	86.5	28	82.6	46	84.0
10	81.2	29	76.7	47	77.2
11	85.1	30	84.3	48	78.9
12	84.2	31	83.0	49	84.5
13	86.0	32	82.9	50	77.2
14	84.4	33	77.0	51	76.8
15	80.5	34	86.0	52	81.2
16	80.2	35	85.9	53	77.1
17	83.5	36	85.1	54	77.7
18	78.3	37	79.7	55	82.2
19	78.9				

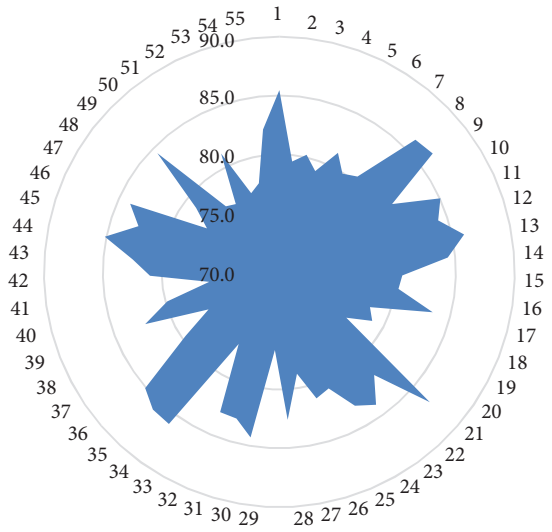

Figure 6: Statistical diagram of the detection effect of the automatic detection method of building cracks based on digital image processing technology and multiscale feature analysis automatic detection algorithm.

5. Conclusion

In order to find out in time whether concrete cracks in construction projects conform to national safety standards and their development and changes, it is necessary to develop a monitor that can accurately monitor the crack width and its changes in real time. It can provide data support for concrete testing results and can also monitor concrete cracks and make effective evaluation after maintenance. In addition, it can also perform construction audits of various materials and components, so it can bring huge social impact. If the crack width of the coagulation map can be automatically detected according to the crack image, the actual work difficulty will be greatly reduced. The reason is that some concrete cracks are in very dangerous places and are difficult to be detected manually. Therefore, it is of certain value and significance to develop an intelligent monitoring system for concrete cracks in construction projects. This paper combines digital image processing technology and multiscale feature analysis automatic detection algorithm to construct an intelligent building structure crack detection system. The experimental results verify that the automatic detection method of building cracks based on digital image processing technology and multiscale feature analysis has a good effect.

Data Availability

The labeled datasets used to support the findings of this study are available from the corresponding author upon request.

Conflicts of Interest

The author declares no competing interests.

Acknowledgments

This study is sponsored by Shandong College of Arts.

References

[1] B. Mou, B.-J. He, D.-X. Zhao, and K.-w. Chau, "Numerical simulation of the effects of building dimensional variation on wind pressure distribution," *Engineering Applications of Computational Fluid Mechanics*, vol. 11, no. 1, pp. 293–309, 2017.

[2] D. Chakraborty and H. Elzarka, "Advanced machine learning techniques for building performance simulation: a comparative analysis," *Journal of Building Performance Simulation*, vol. 12, no. 2, pp. 193–207, 2019.

[3] O. Guerra-Santin and S. Silvester, "Development of Dutch occupancy and heating profiles for building simulation," *Building Research & Information*, vol. 45, no. 4, pp. 396–413, 2017.

[4] T. Dodd, C. Yan, and I. Ivanov, "Simulation-based methods for model building and refinement in cryoelectron microscopy," *Journal of Chemical Information and Modeling*, vol. 60, no. 5, pp. 2470–2483, 2020.

[5] T. Abuimara, W. O'Brien, B. Gunay, and J. S. Carrizo, "Towards occupant-centric simulation-aided building design: a case study," *Building Research & Information*, vol. 47, no. 8, pp. 866–882, 2019.

[6] P. Remmen, M. Lauster, M. Mans, M. Fuchs, T. Osterhage, and D. Müller, "TEASER: an open tool for urban energy modelling of building stocks," *Journal of Building Performance Simulation*, vol. 11, no. 1, pp. 84–98, 2018.

[7] N. Endo, E. Shimoda, K. Goshome, T. Yamane, T. Nozu, and T. Maeda, "Simulation of design and operation of hydrogen energy utilization system for a zero emission building," *International Journal of Hydrogen Energy*, vol. 44, no. 14, pp. 7118–7124, 2019.

[8] I. Beausoleil-Morrison, "Learning the fundamentals of building performance simulation through an experiential teaching approach," *Journal of Building Performance Simulation*, vol. 12, no. 3, pp. 308–325, 2019.

[9] C. Xiong, J. Huang, and X. Lu, "Framework for city-scale building seismic resilience simulation and repair scheduling with labor constraints driven by time-history analysis," *Computer-Aided Civil and Infrastructure Engineering*, vol. 35, no. 4, pp. 322–341, 2020.

[10] A. D. Black, "Wor(l)d-Building: simulation and metaphor at the mars desert research station," *Journal of Linguistic Anthropology*, vol. 28, no. 2, pp. 137–155, 2018.

[11] K. Hanson, L. Hernandez, and J. A. Banaski Jr., "Building simulation exercise capacity in Latin America to manage public health emergencies," *Health security*, vol. 16, no. S1, pp. S98–S102, 2018.

[12] E. K. Wati and N. Widiansyah, "Design of learning media: modeling & simulation of building thermal comfort optimization system in building physics course," *Jurnal Pendidikan IPA Indonesia*, vol. 9, no. 2, pp. 257–266, 2020.

[13] C. W. Lee and S.-J. Cho, "The development of converting program from sealed geological model to Gmsh, COMSOL for building simulation grid," *Journal of the Korean Earth Science Society*, vol. 38, no. 1, pp. 80–90, 2017.

[14] C. Miller, D. Thomas, J. Kämpf, and A. Schlueter, "Urban and building multiscale co-simulation: case study implementations on two university campuses," *Journal of Building Performance Simulation*, vol. 11, no. 3, pp. 309–321, 2018.

[15] X. Xie and Z. Gou, "Building performance simulation as an early intervention or late verification in architectural design: same performance outcome but different design solutions," *Journal of Green Building*, vol. 12, no. 1, pp. 45–61, 2017.

[16] A. I. Adilkhodjayev, I. M. Mahamataliev, and S. S. Shaumarov, "Theoretical aspects OF structural and simulation modeling OF the macrostructure OF composite building materials," *Journal of Tashkent Institute of Railway Engineers*, vol. 14, no. 2, pp. 3–14, 2019.

[17] S. Imam, D. A. Coley, and I. Walker, "The building performance gap: are modellers literate?" *Building Service Engineering Research and Technology*, vol. 38, no. 3, pp. 351–375, 2017.

[18] J.-S. Pei, B. Carboni, and W. Lacarbonara, "Mem-models as building blocks for simulation and identification of hysteretic systems," *Nonlinear Dynamics*, vol. 100, no. 2, pp. 973–998, 2020.